

ARTICLE

Open Access

# Experimental measurement and numerical modeling of deformation behavior of breast cancer cells passing through constricted microfluidic channels

Pouyan Keshavarz Motamed<sup>1,2</sup>, Hesam Abouali<sup>2,3</sup>, Mahla Poudineh<sup>1,2,3</sup> and Nima Maftoon<sup>1,2</sup>

## Abstract

During the multistep process of metastasis, cancer cells encounter various mechanical forces which make them deform drastically. Developing accurate in-silico models, capable of simulating the interactions between the mechanical forces and highly deformable cancer cells, can pave the way for the development of novel diagnostic and predictive methods for metastatic progression. Spring-network models of cancer cell, empowered by our recently proposed identification approach, promises a versatile numerical tool for developing experimentally validated models that can simulate complex interactions at cellular scale. Using this numerical tool, we presented spring-network models of breast cancer cells that can accurately replicate the experimental data of deformation behavior of the cells flowing in a fluidic domain and passing narrow constrictions comparable to microcapillary. First, using high-speed imaging, we experimentally studied the deformability of breast cancer cell lines with varying metastatic potential (MCF-7 (less invasive), SKBR-3 (medium-high invasive), and MDA-MB-231 (highly invasive)) in terms of their entry time to a constricted microfluidic channel. We observed that MDA-MB-231, that has the highest metastatic potential, is the most deformable cell among the three. Then, by focusing on this cell line, experimental measurements were expanded to two more constricted microchannel dimensions. The experimental deformability data in three constricted microchannel sizes for various cell sizes, enabled accurate identification of the unknown parameters of the spring-network model of the breast cancer cell line (MDA-MB-231). Our results show that the identified parameters depend on the cell size, suggesting the need for a systematic procedure for identifying the size-dependent parameters of spring-network models of cells. As the numerical results show, the presented cell models can simulate the entry process of the cell into constricted channels with very good agreements with the measured experimental data.

## Introduction

In addition to several genetic and biochemical factors contributing to the metastatic progression, the biomechanical forces are widely reported to be of considerable importance<sup>1,2</sup>. Among these forces, the

hemodynamic forces play a critical role in metastasis progression, for the blood is the primary route of transporting the circulating tumor cells (CTCs) throughout the body<sup>3,4</sup>. Besides, CTC's survival, intravascular arrest, and extravasation are significantly impacted by shear stresses exerted on them originating from their synchronous interactions with the blood plasma, blood cells, and endothelial cells that form the inner layer of blood vessels<sup>1,5-7</sup>. Despite the crucial importance of the impact of such interactions in the hematogenous spread of metastasis, our understanding is far from complete due to the

Correspondence: Mahla Poudineh ([mahla.poudineh@uwaterloo.ca](mailto:mahla.poudineh@uwaterloo.ca)) or Nima Maftoon ([nmaftoon@uwaterloo.ca](mailto:nmaftoon@uwaterloo.ca))

<sup>1</sup>Department of Systems Design Engineering, University of Waterloo, Waterloo, ON N2L 3G1, Canada

<sup>2</sup>Center for Bioengineering and Biotechnology, University of Waterloo, Waterloo, ON N2L 3G1, Canada

Full list of author information is available at the end of the article

© The Author(s) 2024



**Open Access** This article is licensed under a Creative Commons Attribution 4.0 International License, which permits use, sharing, adaptation, distribution and reproduction in any medium or format, as long as you give appropriate credit to the original author(s) and the source, provide a link to the Creative Commons license, and indicate if changes were made. The images or other third party material in this article are included in the article's Creative Commons license, unless indicated otherwise in a credit line to the material. If material is not included in the article's Creative Commons license and your intended use is not permitted by statutory regulation or exceeds the permitted use, you will need to obtain permission directly from the copyright holder. To view a copy of this license, visit <http://creativecommons.org/licenses/by/4.0/>.

complicated nature of the underlying phenomena. Advanced numerical methods, capable of accounting for the high deformability attribute of CTCs, cell-cell interactions, and interactions with the fluid flow in the delicate microcapillaries have been shown to be promising to decipher CTC's responses to the exerted mechanical forces<sup>8–11</sup>. Priceless knowledge could be acquired by numerically investigating the impact of various sources of mechanical forces on CTCs. Such knowledge helps answer the perplexing question of when, where, and how a secondary tumor can be formed in a distant organ from migrated CTCs<sup>5,12–14</sup>. Furthermore, it enables the development of more accurate diagnostic methods for localizing secondary tumors and the discovery of more efficient treatments for preventing or delaying this deadly disease<sup>12</sup>.

However, for being trustable, a numerical model should numerically replicate the experimentally observed behavior of CTCs<sup>15</sup>. The deformation behavior of CTCs, that greatly affects every step of the metastatic cascade, has been documented to be one of the key characteristics of malignant CTCs in many research studies<sup>1,16–18</sup>. Thus, the deformation behavior of CTCs can be considered as one of the essential behaviors of CTCs that the numerical model must simulate accurately in comparison with the measured experimental data. Besides, numerical modeling of more complex phenomena such as cell-cell interactions, cell adhesion to vessel walls, and extravasation will be affected by the accurate representation of the deformation behavior of CTCs<sup>9,19,20</sup>. This necessitates developing an experimentally validated numerical model of single CTCs' deformation behavior before moving toward modeling more complex phenomena. This requires acquiring precise measurements of single CTC's deformability in a context similar to their microenvironment.

In vivo models that capture the motion and deformation of CTCs in real time are the most relevant models in terms of replicating the microenvironment<sup>5,21</sup>. Although, challenges with in vivo models such as capturing high-resolution images and having precise control of the fluid flow make in vitro models good alternatives for investigating the deformability of cancer cells<sup>12,22</sup>. Since microfluidic devices are the most relevant models in terms of similarity to the blood capillaries among in vitro models, developing advanced microfluidic devices to quantify migratory and deformability capabilities of human cancer cells has attracted many researchers<sup>23–29</sup>. In this regard, shear flow deformability cytometry<sup>30,31</sup> and extensional flow deformability cytometry<sup>32</sup> are the two contact-free approaches that utilize hydrodynamic flow to change the shape of the cells and assess the cell deformability from cell images captured during cell shape change period<sup>33</sup>. Although these contactless cytometry methods can

evaluate cell deformability in a high throughput manner, they are not able to investigate the role of cell-wall interactions on cell deformability. In addition, constricted microfluidic channels whose width are comparable to microcapillary diameters ( $\approx 10 \mu\text{m}$ )<sup>34</sup> became one of the most relevant tools to study the deformability of cancer cells. Using such devices has demonstrated that the entry time, which is the time it takes for the cell to squeeze and fully enter the constriction, would be impacted by the deformability of the cell and is sensitive enough to be different in cancer cells with different levels of malignancy<sup>16,17,28,35</sup>. In addition, since the constricted channel geometry, fluid flow rate, and cells motion are controlled accurately in this type of experiment, it is a good candidate that based on the numerical models of CTC's deformability can be developed and validated. Furthermore, the numerical model is valid when cells are in close contact with the walls of the fluidic domain which could be the case for many practical biomedical applications<sup>21</sup>. More specifically, the cells' entry times calculated from the numerical model can be validated against the experimentally measured ones<sup>8,36–38</sup>.

To date, various numerical methods have been established to quantitatively model the entry process of deformable objects into narrow confinements<sup>37,39–46</sup>. Most precedent models are continuum models which span from liquid drop models to solid models<sup>47</sup> that considered a cell as a viscous fluid encapsulated with the cell's membrane which obeys related constitutive equations<sup>37,39–41</sup>. However, solid models suffer from accurately modeling large deformation of cells, and liquid drop models are insufficient in simulating cell-wall interactions since they assume a lubrication layer between the cell and the constriction walls<sup>41,47–49</sup>. Although solid continuum models with hyperelastic constitutive laws can improve the accuracy of results for large elastic deformation of cells<sup>50,51</sup>, in general, the applicability of continuum cell models for modeling complex biological phenomena have been limited due to their computational inefficiency in dealing with multiple deformable bodies and integration of biochemical interactions at the cellular scale<sup>52</sup>.

To obviate the mentioned drawbacks, spring network models (SNM) of the cell membrane have been devised, progressed, and applied<sup>53–58</sup>. SNM, discretized the cell membrane by a triangular spring network, was devised based on the idea of imitating the physics of the cell membrane by using springs in the numerical model instead of spectrin on the membrane of a red blood cell (RBC)<sup>53,54,59</sup>. High computational efficiency without dropping the model accuracy has been reached with the more advanced SNMs by decreasing the vertices on the cell membrane<sup>55,60,61</sup>. This makes such a method practical for scaling up for simulating circulation, entrapment, and extravasation of CTCs for vessels and organ scale models

of metastasis. Moreover, the computational efficiency and accuracy of SNM over continuum models of RBCs suspended in the fluid was demonstrated<sup>49</sup>. More specifically, a comparison between the computational performance of a spring network model and a continuum linear elastic solid model<sup>62</sup> of RBC proved the higher computational efficiency and higher accuracy of the spring network model over the continuum linear solid model.

However, SNMs have a few unknown model parameters, whose quantities affect the deformation behavior of cells directly, need to be identified for each cell type, cell size, and mesh arrangement to replicate the correspondence experiment accurately. The first efforts of finding these parameters were performed on RBC by either manual adjustment or by making a link between SNM and continuum models<sup>57,63,64</sup>. Since these efforts suffered from unrealistic assumptions in identifying the parameters of RBC, the results were not accurate in replicating the experimental data and other rounds of calibration were required<sup>56,64</sup>. In addition, being highly uncertain in finding the unknown parameters of SNM hinders applying this model to other cell types such as CTCs. Recently, a systematic approach called SNM-GA for identifying SNM parameters has been developed to minimize the error between the experimental data and computational calculation using a genetic algorithm (GA) running on supercomputers<sup>8</sup>. SNM-GA is an inverse method that requires appropriate experimental data that should make the identification step feasible and assure producing a validated numerical model able to simulate the deformation behavior of CTCs robustly. Considering the cells' entry process, the data must be reported as cell's entry time and the quantity must be in the order of milliseconds to help SNM-GA identify the parameters feasibly without needing huge computational resources. Besides, measuring the entry time in various devices with various constriction widths increase the number of inputs and outputs that will be used in the parameter identification step and is the key for developing a robust numerical model<sup>8</sup>. To the best of our knowledge the literature lacks such experimental data that reported the entry time of breast cancer cells in order of millisecond using various micro constriction widths. Therefore, capturing such experimental data was one of the goals of this study.

In this study, we first experimentally investigated the deformability of three different breast cancer cell lines (MCF-7, SK-BR-3, and MDA-MB-231) using a constricted microfluidic device whose constriction width is 10  $\mu\text{m}$ . Then, by focusing on the more deformable one (MDA-MB-231), we extended the experiments to two additional constricted microfluidic devices with 8  $\mu\text{m}$ , and 12  $\mu\text{m}$  widths of constriction. Using SNM, the numerical

models of a single cancer cell passing through constricted channels have been developed. Afterward, the unknown parameters have been identified based on the measured entry times with the use of GA by minimizing the error between computational calculations and the experimental measurements. We demonstrated that by applying the identified model parameters, both the gradual squeezing of the cell into the constricted channels and the shape change of the cell during the entry process could be accurately replicated in-silico. This study is the first study to present a valid discrete numerical model for the deformation behavior of highly metastatic cancer cells (MDA-MB-231) for a range of cell diameters. The presented models can be used as the foundation of discrete models of the motion and deformation of circulating breast cancer tumor cells upon which numerical models of more complex phenomena such as cell-cell interactions, and CTC cluster deformation behavior in microcapillaries can be built.

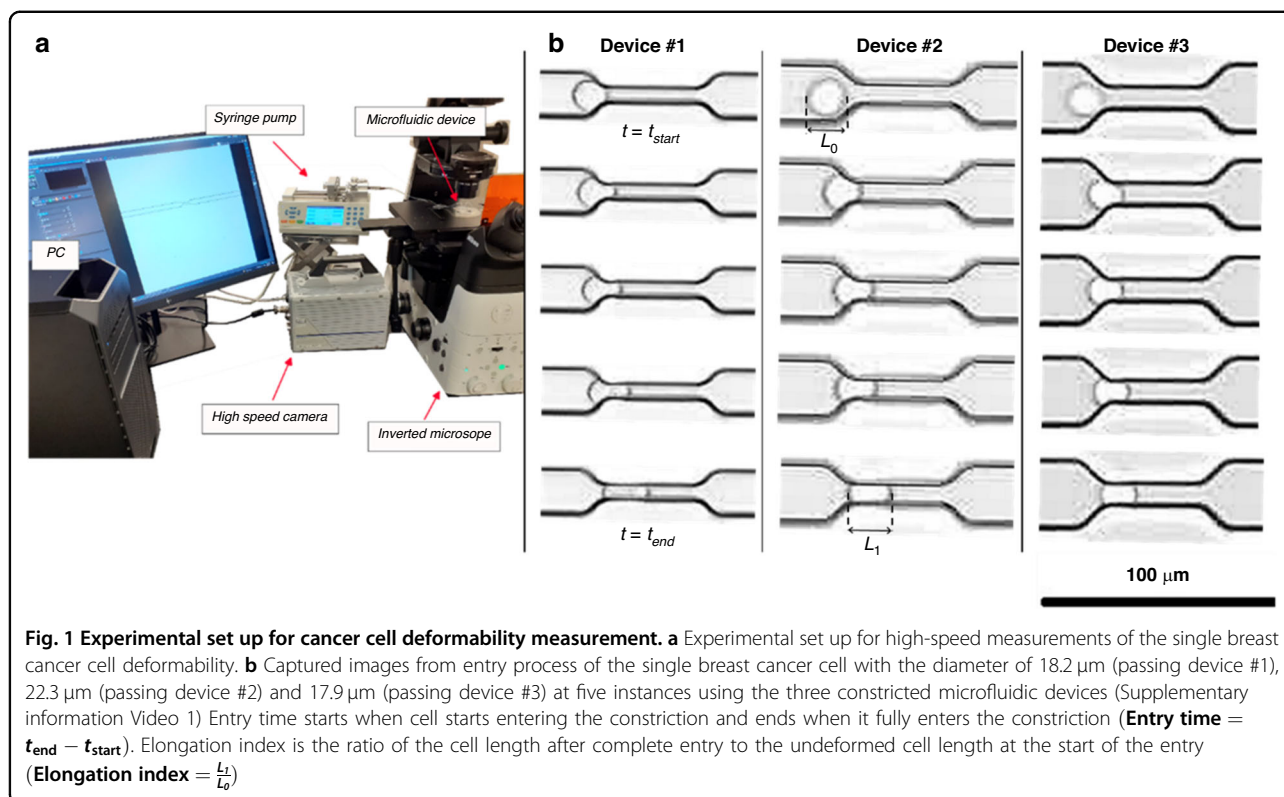
## Results and discussion

### Experimental measurement

In this study, to investigate the deformation behavior of breast cancer cells in a microcapillary similar to that of CTCs passing confined spaces, we measured the entry process of the cells entering narrow constricted microfluidic channels. Samples of captured images of the entry process of cancer cells (MDA-MB-231) in all three microfluidic devices (Device #1 to Device #3 from left to right) at five instances are shown in Fig. 1. As shown in Fig. 1b, the entry time starts when the cell starts entering the constriction and ends when the cell fully enters the constriction. In addition, the elongation index, is defined as the ratio of the cell length after completing the entry to the constriction to the original length of the cell before the start of the entry process as shown in Fig. 1b. The images were selected to show similar location and deformation of the cells, but the timing of the squeezing process is different in each device as detailed below.

First, we compared the cell deformation behavior of different breast cancer cell lines MCF-7, SK-BR-3, and MDA-MB-231 with moderate to high metastatic potential<sup>65</sup> (Fig. 2). In Fig. 2a, each point represents one measured cell. As measured data in Fig. 2a show the entry times of all cell lines are increasing exponentially

as the cell diameter increases. A comparison between the exponential rate of the best-fit curves of all three cell lines discloses that the entry time of MDA-MB-231 is less sensitive to the increase of cell diameter than the other two cell lines. In addition, entry times of highly invasive breast cancer cells (MDA-MB-231) are shorter than the other two cell lines for a given cell size as the exponential fits in Fig. 2a shows. Taking the cell diameter of 18  $\mu\text{m}$ , the entry times of MDA-MB-231, SK-BR-3, and MCF-7



according to exponential fits in Fig. 2a are 10.6 ms, 16.2 ms, and 27.4 ms, respectively. Figure 2b shows the average entry time for all cell sizes is also shorter for the MDA-MB-231 cell than it is for the other two cell lines.

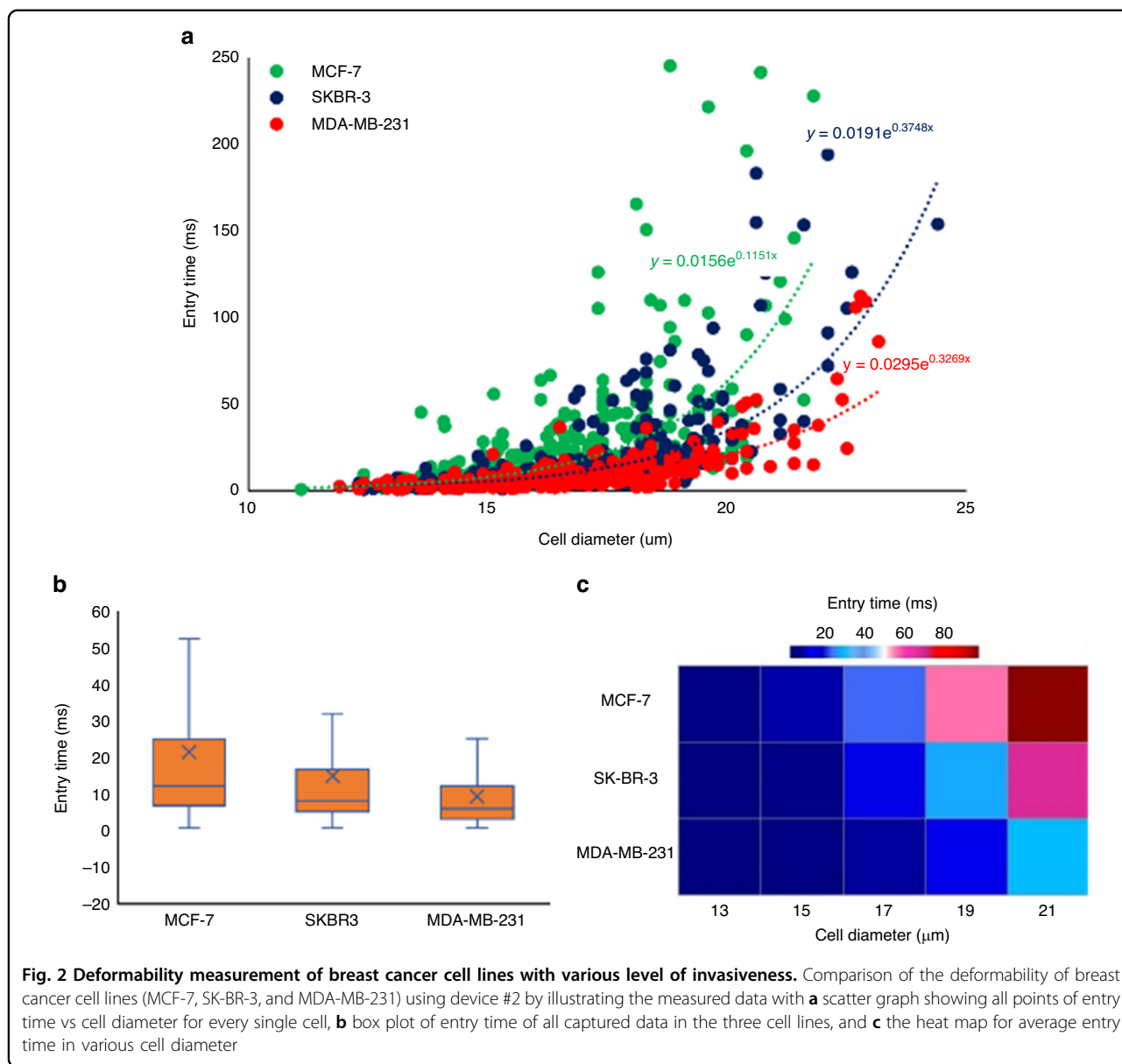
This confirms that the entry time can be a good index to measure the mechanical deformability of cancer cells with various levels of invasiveness<sup>13,14</sup>. Figure 2c illustrates the average entry time for various cell sizes (ranging from 13–21  $\mu\text{m}$ ) of the three cell lines. This figure indicates the difference in the deformability of the three cell lines becomes visible for cell sizes greater than 17  $\mu\text{m}$ . The results in Fig. 2 demonstrate higher deformability of MDA-MB-231 cell line compared to the other two cell lines consistent with the studies that reported it to be capable of metastasizing in vivo when it is directly injected to the circulatory system<sup>57</sup>.

Because the deformation behavior of MDA-MB-231 cells entering a narrow channel is closer to that of CTCs passing confined microcapillaries than the other two cell lines, we focused on expanding the deformability measurements of this cell line to also use the data for developing validated SNMs of breast cancer cells. More specifically, we measured the entry time and elongation index of MDA-MB-231 passing through the constricted channel of all three microfluidic devices fabricated in this study. Figure 3 shows the measured entry time for different cell sizes as well as exponential fits for the three

devices. The data in Fig. 3 show that for a fixed cell diameter, the entry times and the elongation indexes of the cell passing a wider constricted channel are smaller. For instance, the fitted curves in Fig. 3a show the entry time for an 18  $\mu\text{m}$  MDA-MB-231 that was measured using Device #1, Device#2, Device#3 is 15.1, 10.6, and 6.4 ms, respectively. In addition, the elongation indexes of 18  $\mu\text{m}$  MDA-MB-231, calculated from the fitted curves in Fig. 3b, are 1.27, 1.18, and 1.11 using Device #1, Device #2, and Device #3, respectively.

#### Parameter identification and numerical results

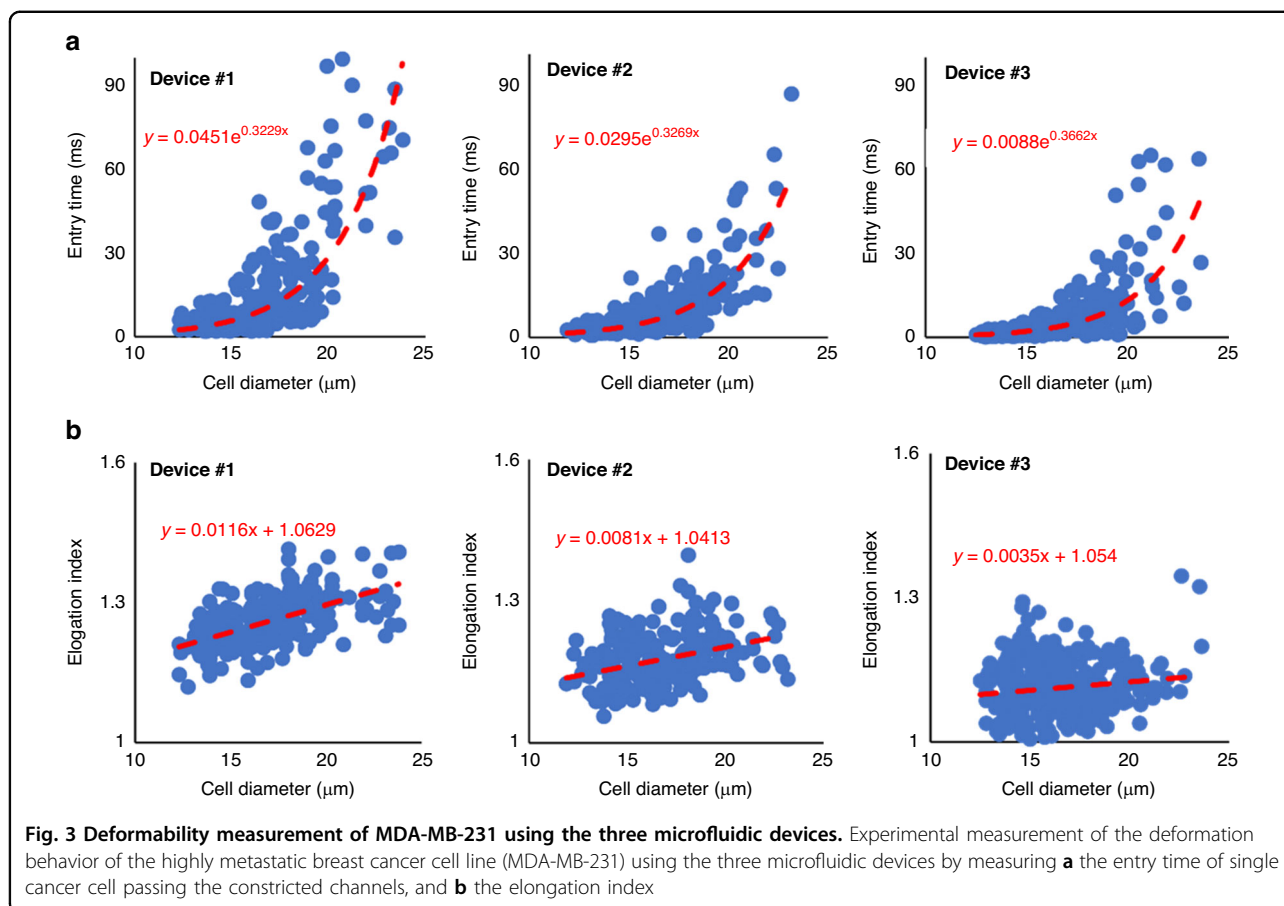
The deformability of the cells can be captured using the SNM if the correct model parameters are identified. Using the GA, as described in Materials and Methods, we identified the unknown model parameters utilizing the fitted curves to the measured entry times of MDA-MB-231 for 6 different cell sizes between 13  $\mu\text{m}$  to 18  $\mu\text{m}$  in the three microchannel devices (in Fig. 3). In this study, for each cell size the identification procedure was performed using the experimental data of that cell size separately to increase the identification accuracy. For the MDA-MB-231 cancer cell with the diameter of 16  $\mu\text{m}$ , the evolution of the error function (Eq. 11) considering all three microchannel devices for the best set of parameters at every generation is shown in Fig. 4a. The numerically calculated entry times in each of the three microchannel devices using this GA



process are shown in Fig. 4b. As Fig. 4a shows, for this cell size, the error got close to an optimum value after four generations, improved between generations 5–12, and remained unchanged after the 12th generation. Figure 4b shows that convergence of the entry times follows the same trend as the error function in Fig. 4a.

Figure 4c–e shows five instances of the simulated entry process of the 16 μm cell after applying the identified quantities for the unknown parameters of the cell model in three devices. The time instances in these panels are different but were selected to show comparable squeezing state between the three devices. The shape of the cell and its interaction with fluid and microfluidic walls are illustrated from two different views as the cell enters the

constricted channel in each microfluidic device. The streamlines in these figures visualize the fluid flow interactions with the squeezing cell and the walls of the devices. Streamlines experience the greatest disturbance in Device #1, where the greatest size mismatch between the cell and constricted channel sizes exists. The disturbance is the most visible in the two last time instances (two rightmost) of Fig. 4c when the cell is near to complete entry to the constricted channel. The same cell size causes a minimal disturbance in the streamlines in Device #3 close to the complete entry state (two leftmost states in Fig. 4e). Supplementary Videos 2 to 4 show the squeezing process of Fig. 4c–e with a higher temporal resolution. The parameter values, that reached the best rank at each



generation for 16  $\mu\text{m}$  cells, are given in Table 1. Moreover, the results of the identification step including the identified parameter values and the minimized error of every cell size are summarized in Table 2.

The model should be able to replicate the motion and deformation of the population of cells observed experimentally. To verify this, we quantified the numerically calculated entry time and elongation index of the cell after complete entry and compared them with ones obtained experimentally for the population of MDA-MB-231 cells in all three devices represented by the fitted curves in Fig. 5 (reproduced from Fig. 3).

The numerical calculation used the identified parameters reported in Table 2. Figure 5 shows that the numerically obtained entry times and the shape of the cells (characterized by the elongation index at full entry to the constriction) closely replicate the motion and deformation of the population of the cell observed experimentally. The average errors among all devices and cell sizes were 13% for the entry time and 1.4% for the elongation index at full entry to the constriction.

Moreover, in Fig. 6, the numerical and experimental results of the axial cell position and evolution of the cell

length during the entry process of MDA-MB-231 in Device #2 were compared. In this figure, data for cell diameters of 13, 15 and 18  $\mu\text{m}$  are presented. Figure 6a shows that increasing the cell diameter makes the cell squeezing into the constriction longer and this behavior was consistently observed in experimental and numerical data. Furthermore, the validated numerical model closely reproduced the experimental observations. Figure 6b shows the gradual and consistent increases in the cell length calculated from the numerical model are very similar to that of the experiment for all three cell sizes. In addition, these observations can also be seen in similarly, Supplementary Videos 5–7 show squeezing of cancer cells into the microchannel, increasingly decelerates the cell motion with increasing the diameter from 13 to 18  $\mu\text{m}$  in the same constricted channel (Device #2). Figure 6c illustrates the axial cell position and cell length at 4 different time steps during cell entry.

We used this validated model to obtain the deformation behavior of the cancer cell in terms of cell length and cell center trajectory using all identified cell model with different sizes (Table 2) that are numerically investigated in detail in Fig. 7. This figure shows that increasing the cell

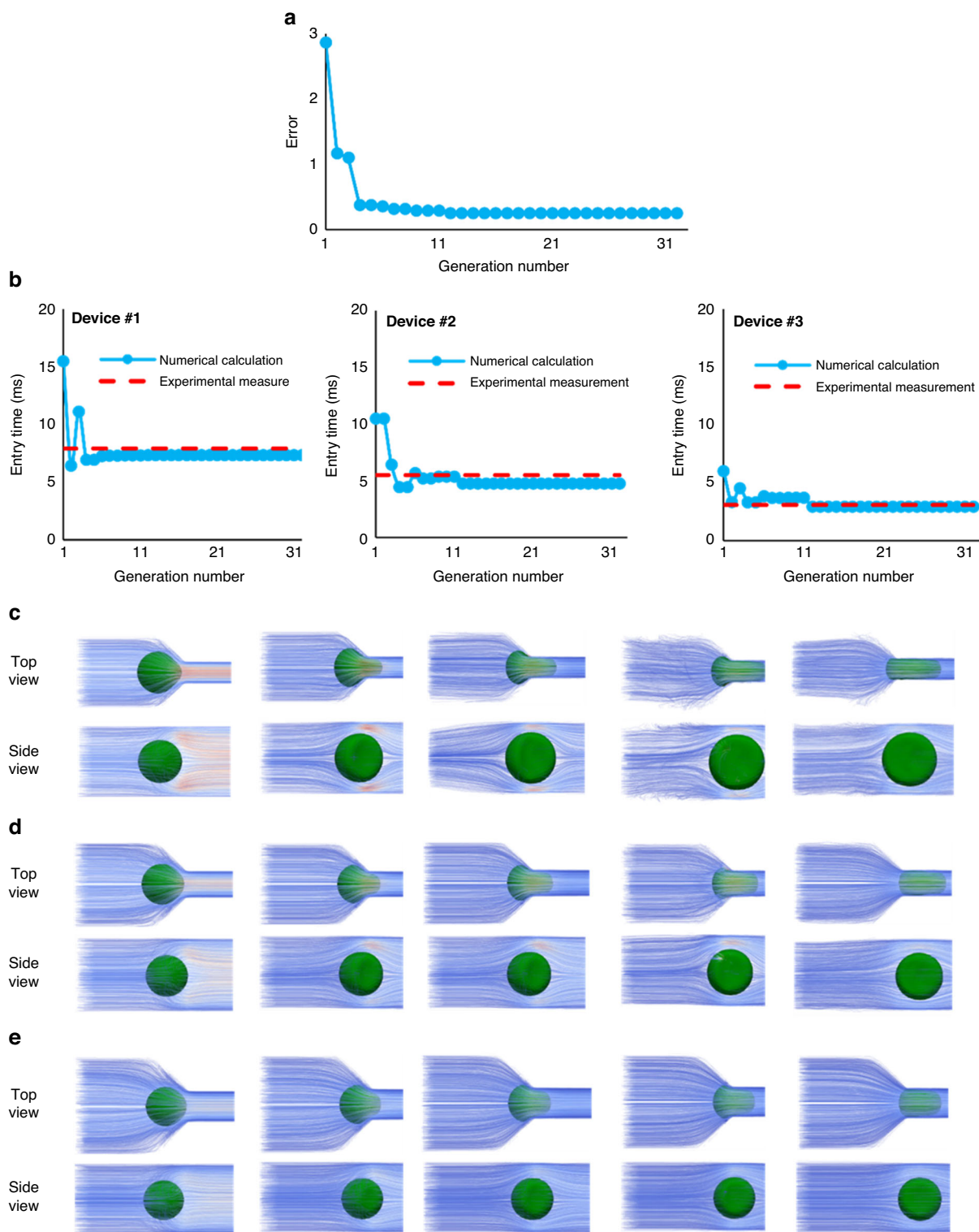


**Fig. 4** Cell model parameter identification of the 16  $\mu\text{m}$  cell using GA. **a** Error minimization for the cell entry time completed after 32 successive generations. **b** Entry time convergence to the experimental values in the three devices shown at every generation. **c–e** The numerical simulations of the entry process of the cell entering the constricted channels after applying the identified parameters for the cell model in the three devices illustrated at five instances in two different views. (Supplementary information Video 2 to Video 4)

**Table 1 The quantities of the 16  $\mu\text{m}$  cell model parameters for the best ones at each generation**

Generation	$K_b$	$K_v$	$K_a$	$K_l$	VR	$E_1$	$E_2$	$E_3$	Error
1	79,675	34,530	31,834	80,957	1.2	0.960911	0.905116	0.94585	2.811876
2	84,715	49,604	46,274	95,927	2.2	0.185705	0.905116	0.081388	1.172209
3	53,904	49,983	9980	18,070	16.9	0.40797	0.170537	0.464981	1.104359
4	383	70,593	33,096	20,175	13.8	0.120177	0.191038	0.06939	0.380605
5	383	70,593	33,096	20,175	13.8	0.120177	0.191038	0.06939	0.380605
6	52,948	23,342	1014	30,366	10.2	0.081467	0.0332	0.247082	0.361749
7	65,639	24,273	35,053	18,419	19.9	0.07704	0.050798	0.192931	0.320769
8	65,639	24,273	35,053	18,419	19.9	0.07704	0.050798	0.192931	0.320769
9	45,361	92,626	20,013	22,461	19.2	0.072106	0.021771	0.20201	0.295887
10	45,361	92,626	20,013	22,461	19.2	0.072106	0.021771	0.20201	0.295887
11	45,361	92,626	20,013	22,461	19.2	0.072106	0.021771	0.20201	0.295887
12	45,526	93,182	19,816	23,203	19.9	0.070715	0.132257	0.050584	0.253555

**Table 2 The quantities of the identified parameters for various cell sizes ranging from (13–18  $\mu\text{m}$ )**

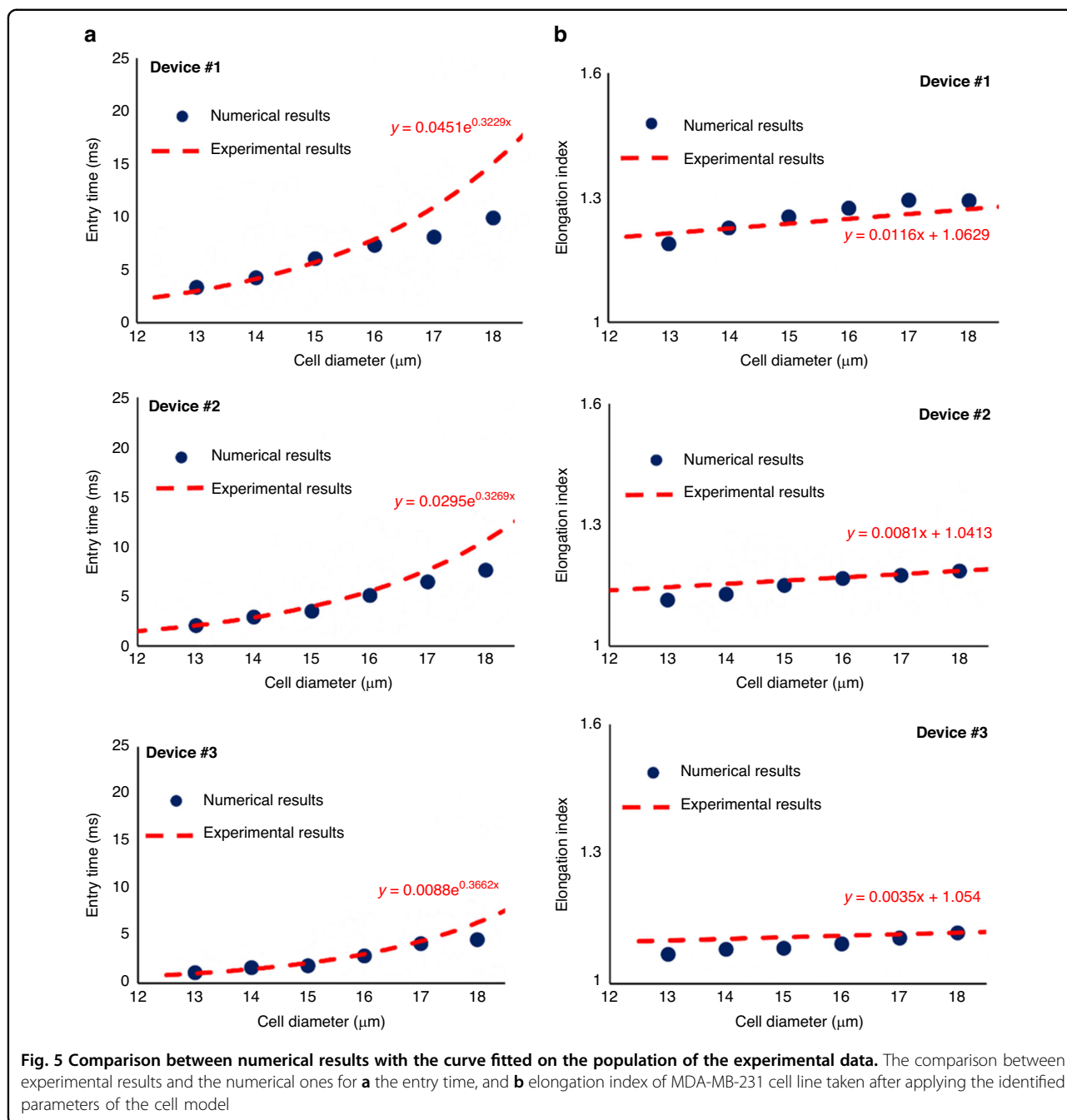
Cell diameter ( $\mu\text{m}$ )	$K_b$	$K_v$	$K_a$	$K_l$	VR	Error
13	98,769	90,341	10,028	22,644	3.8	0.21
14	96,514	47,006	15,056	18,458	14.9	0.17
15	64,763	45,165	79,571	8854	39.9	0.30
16	45,526	93,182	19,816	23,203	19.9	0.25
17	52,542	110	19,948	29,936	37.2	0.51
18	12,109	1420	6958	33,000	21.9	1.07

size within one device increasingly decelerates the cell squeezing making the entry time increasingly longer. As an example, in Device #1, the entry time goes up from 4 ms to 10 ms when the cell diameter changes from 13  $\mu\text{m}$  to 18  $\mu\text{m}$ . On the other hand, increasing enlargement of the constricted channel from Device #1 to Device #3 (from 8  $\mu\text{m}$  to 12  $\mu\text{m}$ ) increasingly shortens the entry time from the maximum 10 ms for 18  $\mu\text{m}$  cell in Device #1 to ~6 ms for the same cell size in Device #3. Figure 7b shows that the most drastic cell-shape change (5  $\mu\text{m}$  increase in the cell length) occurs with the most cell-channel size mismatch (18- $\mu\text{m}$ -diameter cell in 8- $\mu\text{m}$  channel of Device #1). Consistently, the least cell-shape change (0.5  $\mu\text{m}$  increase in the cell length) occurs with the least cell-channel size mismatch (13- $\mu\text{m}$ -diameter cell in 12- $\mu\text{m}$  channel of Device #3). Within one channel size, increasing the cell diameter increases the cell deformation. For example, in Device #1, cells of diameters 13  $\mu\text{m}$  and 18  $\mu\text{m}$  experience 3.5  $\mu\text{m}$  and 5.3  $\mu\text{m}$  length change,

respectively. In addition, using the validated 3D cell models, the effect of changes in the channel height on the entry time of cells with different sizes was investigated (Fig. 8). As Fig. 8 illustrates, for the same fluid flow rate (20  $\mu\text{L}/\text{h}$ ) flowing through the 10  $\mu\text{m}$  width constriction, increasing the channel height decreases the fluid velocity in the channel, and as a result the cell entry time nonlinearly increases for all three cell sizes. As an example, for the 16  $\mu\text{m}$  cell, increasing the channel height from 22  $\mu\text{m}$  to 30  $\mu\text{m}$  caused the entry time to increase nonlinearly from 2.4 ms to 6.9 ms. Figure 8b shows the side view of the entry process of 18  $\mu\text{m}$  cancer cell at three instances (start, middle and end of cell entry) entering the constricted channel of device #2 with various channel height. The physical time of these shown instances were different, but all are captured at the comparable instant of the entry process. As this figure shows, the decrease in the fluid velocity magnitude due to increasing the channel height can be noticed specially at the back and front of the cell that illustrates the decrease in cell velocity.

Since in the present model the FSI is a two-way communication between the cell and fluid at each time step<sup>58</sup>, the model is capable of calculating the time-dependent effect of the cell entry process on the fluid flow rate in the microchannel. In fact, capturing the effects of the fluid motion on the cell deformation can help unraveling the impact of hemodynamics on the hematogenous spread of metastasis<sup>6</sup>. Figure 9a shows the changes in the flow rate as a cell squeezes in the constricted channels of the three devices for three cell sizes. In all devices and cell sizes shown in Fig. 9a, the initial flow rate of 20  $\mu\text{L}/\text{h}$  starts to drastically drop as cell squeezing starts and progresses but the rate and magnitude of the drop depends on the cell

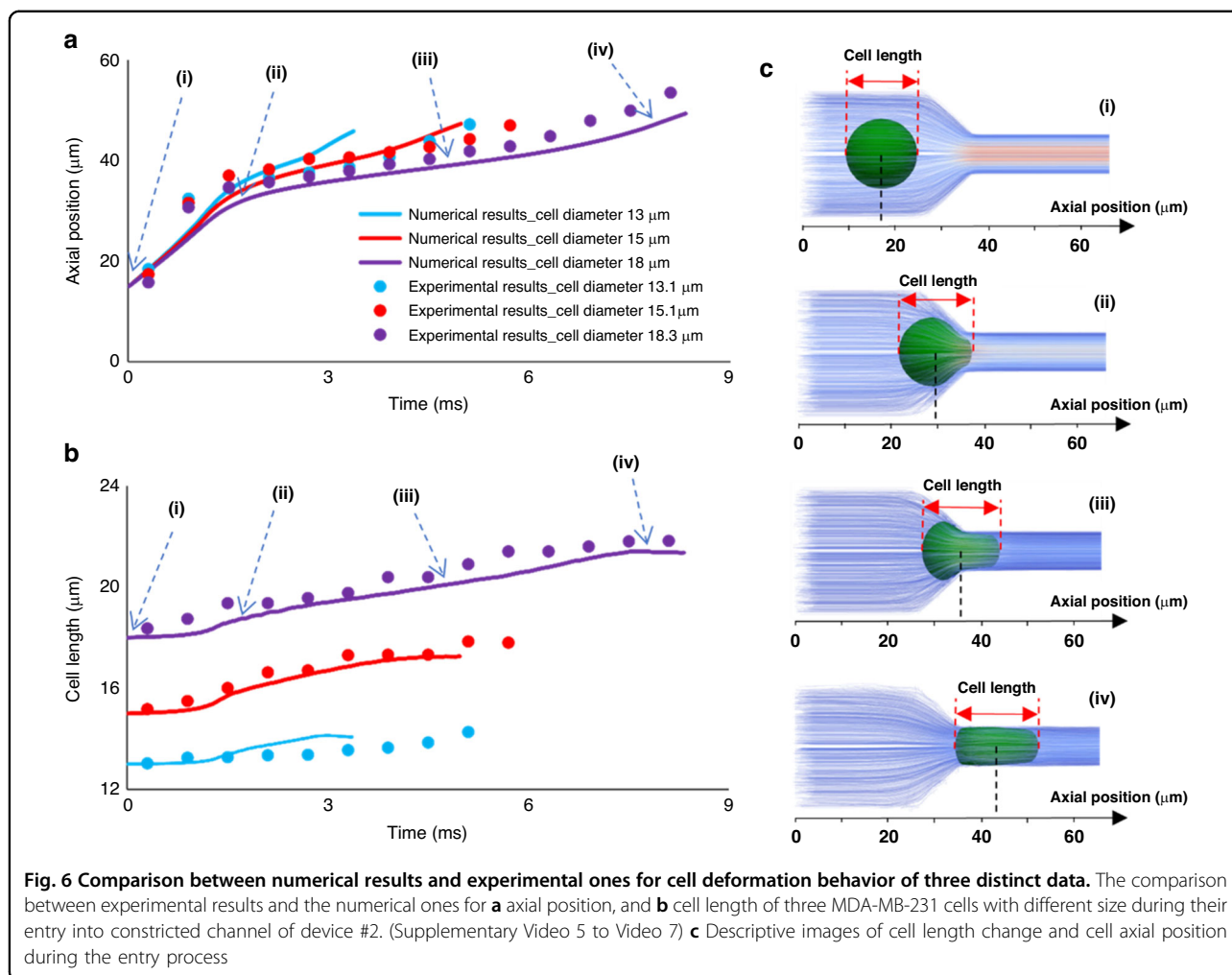




and microchannel sizes. For example, for the cell diameter of 18  $\mu\text{m}$  in Device #1 the flow rate decreases to 0.7  $\mu\text{L/h}$  while the lowest flow rate in this device for 16  $\mu\text{m}$  cell and 14  $\mu\text{m}$  cell are 3.3  $\mu\text{L/h}$  and 7.4, respectively. Besides, the constricted channel width affects the fluid flow rate decrease during the entry process as for 18  $\mu\text{m}$  cell in Device #2 and Device #3 the flow rate reaches as low as 3.8  $\mu\text{L/h}$ , and 5.8  $\mu\text{L/h}$ , respectively.

Figure 9b shows the effect of the flow rate on the entry time of the cell. For the flow rates more than 40  $\mu\text{L/h}$ , the

entry times of three different cell sizes (14, 16, 18  $\mu\text{m}$ ) are almost the same in the constricted channel of all three devices. For instance, the numerically calculated entry times for cell diameters of 14, 16, and 18  $\mu\text{m}$  that pass the constriction in Device #1 with 40  $\mu\text{L/h}$  flow rate are 1.4 ms, 1.8 ms, and 2.3 ms, respectively. As the flow rate decreased from 40  $\mu\text{L/h}$  to lower values, the effects of the cell and microchannel sizes become increasingly more remarkable. For example, in Device #1 with the flow rate of 20  $\mu\text{L/h}$  the entry times of 4.2, 7.3, and 9.6 ms

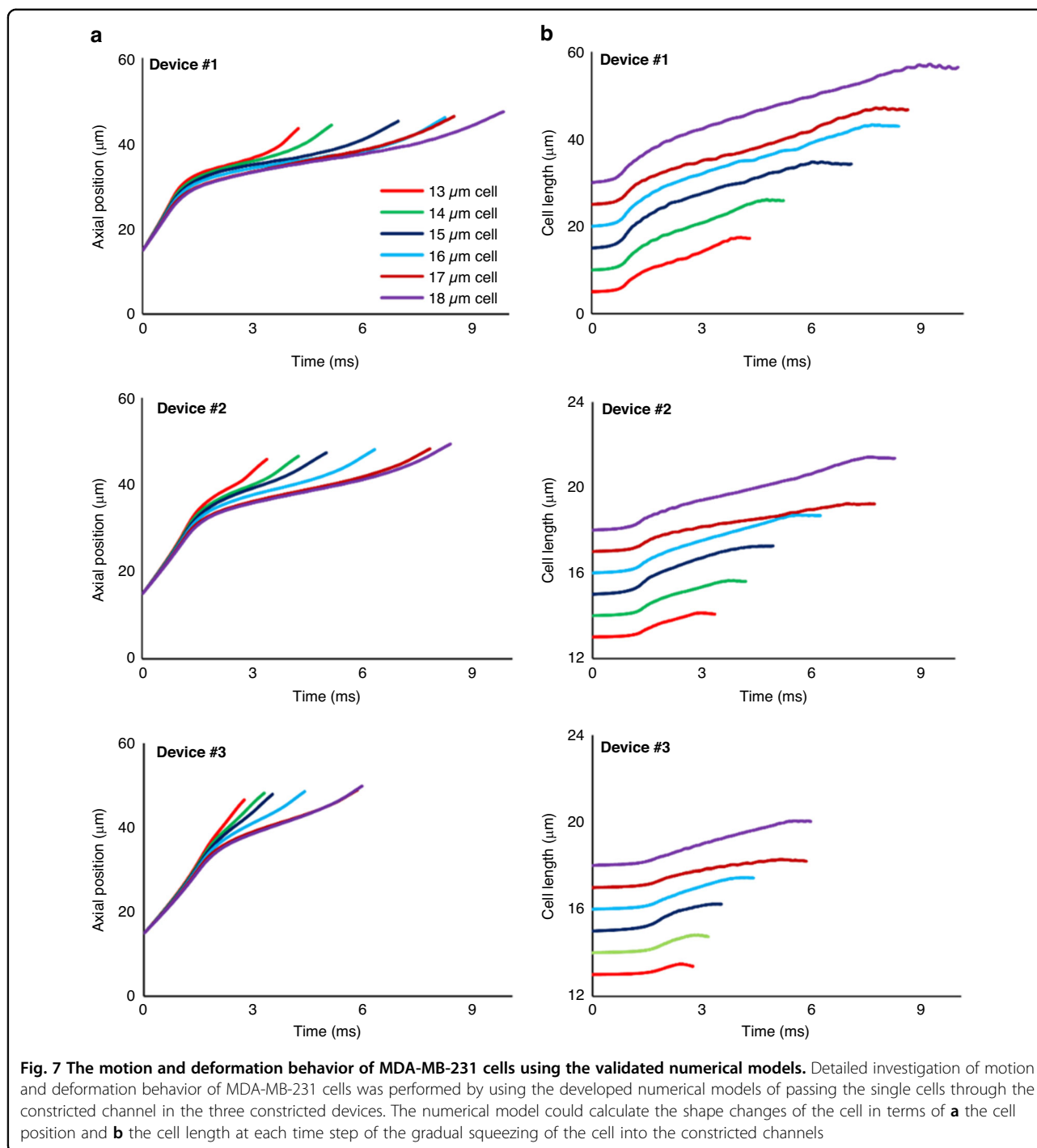


were calculated. However, in Device #3 at the flow rate of  $10 \mu\text{l/h}$  the entry times of cells with the diameters of  $14 \mu\text{m}$  and  $18 \mu\text{m}$  was calculated to be  $6.1 \text{ ms}$  and  $18.3 \text{ ms}$ , respectively.

## Conclusion

This study investigated the feasibility of numerically replicating the deformation behavior of single CTCs passing confined spaces in microcapillaries using an advanced in-silico method at the cellular scale. The proposed SNM-based in-silico method was enabled by the previously developed optimization code that encapsulates the experimental data in a validated model of cancer cell deformation. For simplicity, this study used experimental deformation of cancer cell lines in vitro in constricted microfluidic devices instead of studying real CTC deformations in real human microcapillaries. In the first step of this study, the deformability of three different breast cancer cell lines (MCF-7, SK-BR-3, and MDA-MB-231) was measured. The results show the highly metastatic cell

line (MDA-MB-231) is the most deformable one among the three confirming this cell line merit for using as CTCs' replica in the in-vitro experiments. Therefore, the optimization algorithm for parameter identification of the cell membrane model was applied to the experimental results of the deformability of highly metastatic breast cancer cells (MDA-Mb-231) passing constricted microfluidic devices with various widths of the constricted channel (ranging from  $8$  to  $12 \mu\text{m}$ ). The parameter identification step, which was performed on various cell sizes (ranging from  $13$  to  $18 \mu\text{m}$ ), helps achieve accurate results for the deformation behavior of discrete cell models in a range of cell diameters. The numerical results show good agreements with the experimental ones in terms of both the entry time and elongation index in various geometrical domains. This means that the results of the numerical models are valid for both the gradual squeezing of the cell into the constrictions and the shape of the cell during the entry process. To the best of our knowledge, this study is the first one to present a valid discrete



numerical model for the deformation behavior of highly metastatic cancer cells (MDA-MB-231) for a range of cancer cell diameters. The agreement between numerical and experimental results for large deformation of highly metastatic cancer cells opens doors for further investigations of complex biological phenomena that are instrumental in the hematogenous spread of metastasis with the use of the proposed method. Since the mechanical

properties of each cancer cell type is different from other cancer cell types, the combined experimental-numerical method, proposed in this work, can be used to obtain the valid model specific to that cell type. Such models can be used to investigate the situation in which cancer cells physically occlude a microcapillary or adhere to a vessel wall can be studied by applying the validated model presented here. Furthermore, the motion and deformation

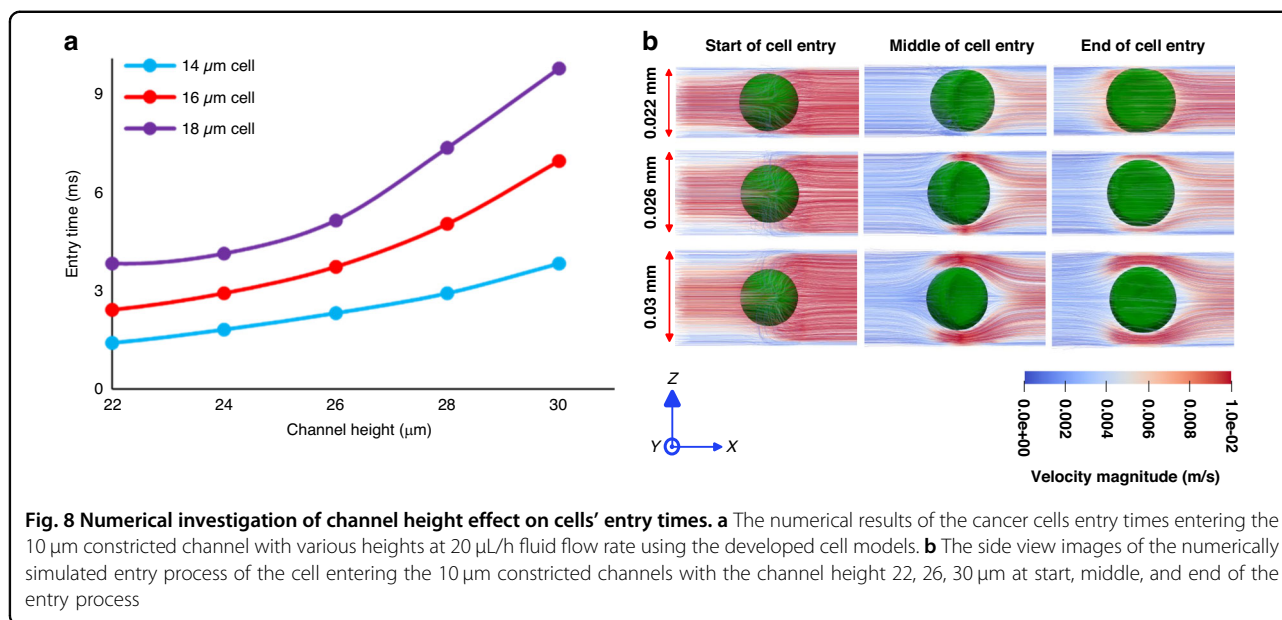


**Fig. 8 Numerical investigation of channel height effect on cells' entry times.** **a** The numerical results of the cancer cells entry times entering the  $10\ \mu\text{m}$  constricted channel with various heights at  $20\ \mu\text{L/h}$  fluid flow rate using the developed cell models. **b** The side view images of the numerically simulated entry process of the cell entering the  $10\ \mu\text{m}$  constricted channels with the channel height  $22, 26, 30\ \mu\text{m}$  at start, middle, and end of the entry process

behavior of CTC clusters can be numerically obtained by repeating the presented approach for CTC clusters. Finally, measuring CTCs deformability acquired from the liquid biopsy in patients and developing the numerical model based on the deformability of real CTC data can advance the numerical model to a higher level for potential future clinical applications.

## Materials and methods

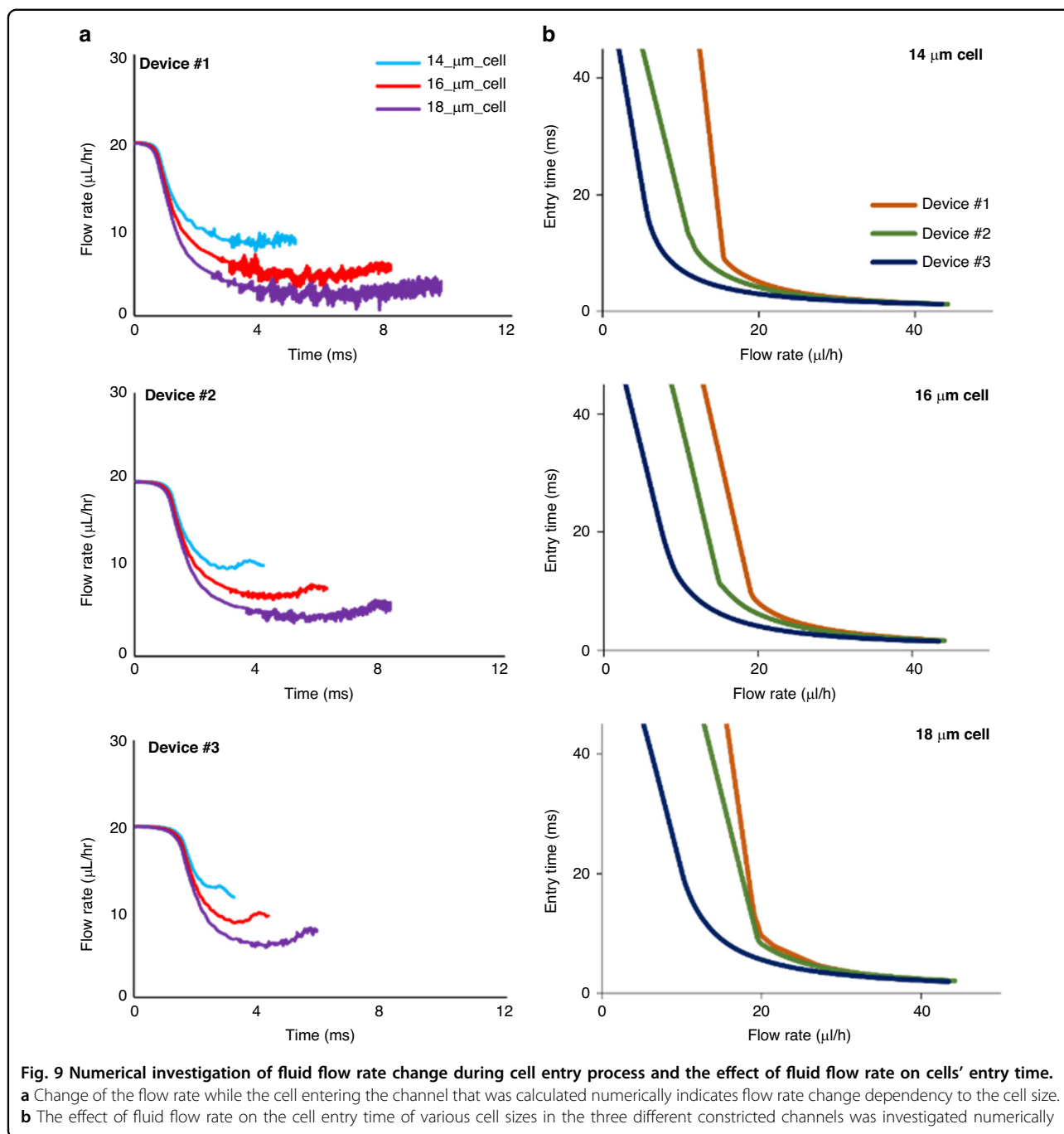
### Cancer cells culture

Immortalized breast cancer cell vials (MCF-7, SK-BR-3, and MDA-MB-231 cell lines with moderate to high metastatic potential<sup>65</sup>) were taken out from storage and cultured in Dulbecco's Modified Eagle Medium, DMEM, (4.5 g/L glucose, with L-glutamine & phenol red without sodium pyruvate, WISENT Inc.) supplemented with 10% v/v of fetal bovine serum (WISENT Inc.) and 1% v/v of streptomycin (WISENT Inc.) in  $75\ \text{cm}^2$  T-flasks (Thermo Fisher Scientific). Cells were incubated in a standard humidified incubator at  $37\ ^\circ\text{C}$  and 5%  $\text{CO}_2$ . Cells upon reaching a confluency of more than 70% were detached and passaged. On the day of the experiment (half an hour before the experiments), cells were detached with 0.25% trypsin-EDTA (WISENT Inc.) after three or less passages. Cells were quantified for their viability with trypan blue with an automated cell counter (Olympus Life Science). Two to four million cells per mL were grown and used for every experiment.

### Design, fabrication, and characterization of microfluidic devices

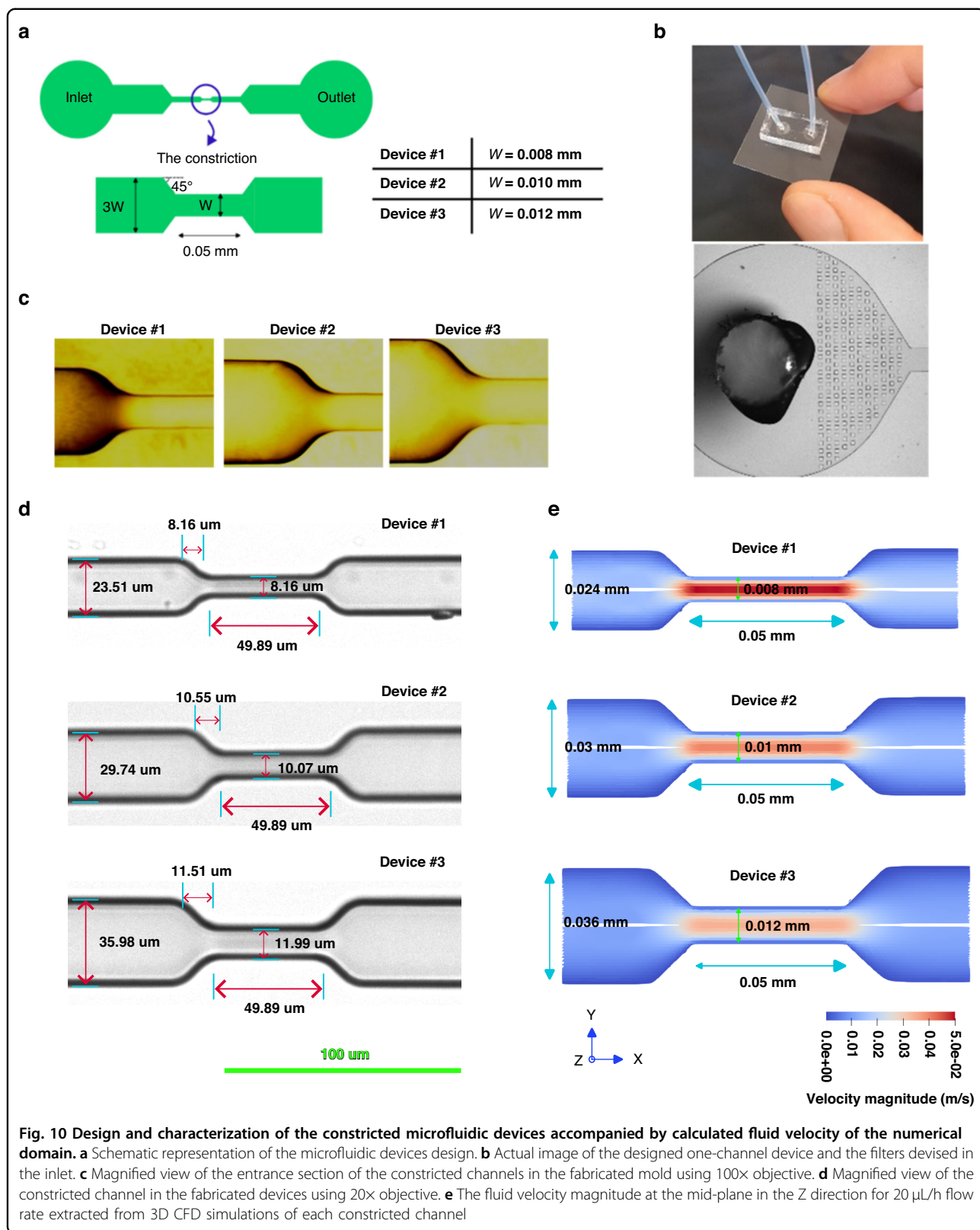
The design of microfluidic devices contains a single constricted channel in the middle with sizes comparable

to human microcapillaries to assure cell deformation at the constrictions' entrance (Fig. 10a, b). The microfluidic devices were fabricated using soft lithography techniques. One layer master mold was fabricated by spin coating SU-8 photoresist 2015 (Kayaku Advanced Materials) at 1400 rpm for 30 s on a silicon wafer. After spin-coating, the wafer was soft baked at  $65\ ^\circ\text{C}$  for 1 min followed by  $95\ ^\circ\text{C}$  for 4 min, and  $65\ ^\circ\text{C}$  for 1 min. Then, the photoresist was exposed to UV light using Karl Suss MA6 Mask Aligner through a previously designed and fabricated chromium glass mask (Nanofab, Alberta University) for 6 s. Next, the post-exposure bake was performed similar to the soft bake procedure. Then, the wafer was developed for 5 min with a SU-8 developer and located on a hot plate at  $150\ ^\circ\text{C}$  for 20 min to stabilize the SU-8 microstructures. The microscopic images of the constricted channels patterned in the master mold are shown in Fig. 10c. In addition, the height of the microchannels was measured to be  $28\ \mu\text{m}$  using a surface profilometer (Dektak 8 Stylus Profilometer). After fabricating the silicon master mold, polydimethylsiloxane (PDMS) monomer and curing agent were mixed at a 10:1 volumetric ratio. Then, the mixture was degasified in the desiccator, poured on the silicon master, and thermally cured at  $70\ ^\circ\text{C}$  for 2 h. The cured PDMS was stripped off from the silicon master. Then, the cured PDMS containing the constricted microchannel replicas were cut to the appropriate size, punched in the inlets and outlets to obtain the fluidic access holes, and bounded to a glass slide using oxygen-plasma bonding. The device fabrication was completed by connecting silicon tubing secured with glue to the fluidic access holes. To characterize the critical features of the microfluidic devices, bright field images of the constricted channel of



all devices captured by an inverted microscope (Nikon Ti Eclipse) were analyzed. Using a 20 $\times$  objective, magnified images of the constricted channels, constriction entrance, and exit portion were captured and measured. As Fig. 10a, d show three constricted devices each of which has a 45 $^\circ$  tapered entrance at the constricted channel, whose width is comparable to microcapillary diameters ranging from 8 to 12  $\mu\text{m}$ <sup>34</sup>, that fabricated and used in this study. Moreover, comparing to the constricted channels used in the literature<sup>16,17,38</sup>, measuring cell deformability with cell

diameter ranging from 13  $\mu\text{m}$  to 26  $\mu\text{m}$ , the fabricated constricted channels in the present study made measuring the single-cell deformability of almost all sizes of the targeted cancer cells feasible. In each device, the width of the channel before the constricted channel is 3 times larger than the width of the constricted channel. This assures both the device fabrication with accurate features and keeping the numerical domain small enough for performing the parameters identification. It is worth mentioning that cell samples were not filtered prior to



infusing into the microfluidic devices, but square shape filters with 50  $\mu\text{m}$  distance from each other were devised in the inlet of each device to help reducing cell aggregate at the constricted channel (Fig. 10b).

## Numerical method

### Lattice Boltzmann method (LBM)

The entry process of a single cancer cell into the constricted channels was modeled using Hemocell open-source code (version 2.4)<sup>57</sup>. In this code, the fluid is considered as an incompressible Newtonian fluid whose motion is described in a Eulerian framework and solved by Lattice Boltzmann Method (LBM) implemented in Palabos open-source code (version 2.0)<sup>66</sup>. More specifically, a three-dimensional 19-velocity cube lattice scheme (D3Q19) is utilized in the LBM governing equations as follows:

$$n_i(x + e_i \Delta t, t + \Delta t) = n_i(x, t) - \frac{1}{\tau} (n_i(x, t) - n_i^{eq}(x, t)) + f_i(x, t) \text{ for } i = 1, 2, \dots, 19 \quad (1)$$

where  $n_i(x, t)$ ,  $e_i$ ,  $\Delta t$ ,  $\tau$  and  $f_i(x, t)$  are the density distribution function, the velocity vector, time step, relaxation time toward the equilibrium distribution  $n_i^{eq}$ , and external force, respectively. At each lattice

site, the macroscopic fluid density  $\rho$  and velocity  $u$  can be obtained from the particle density functions as follows:

$$\begin{aligned} \rho(x, t) &= \sum_i n_i(x, t) \text{ for } i = 1, 2, \dots, 19 \\ \rho(x, t)u &= \sum_i n_i(x, t)e_i \text{ for } i = 1, 2, \dots, 19 \end{aligned} \quad (2)$$

The numerical domains of the three constricted microfluidic devices (shown in Fig. 10a, d) have been created and meshed in a CAD software (Salome 9.7.0)<sup>67</sup> and the fluid passing through each microchannel was modeled using the above described LBM implementation in Hemocell and Palabos. Figure 10e shows fluid flow simulation at the mid-plane along height direction (z-axis) in three microfluidic devices. Moreover, both the channels' geometry and the geometrical domain in x-y plane that used for numerical simulation of the cell entry process in the constricted devices were shown in Fig. 10e.

### Cell Membrane Model

The cancer cell is considered as a membrane with a spherical shape which is discretized by two-dimensional triangles with springs on the triangles' edges. The constitutive equations governing the deformation behavior of the cancer cell include a set of forces (the link force, the bending force, the local area force, and the volume force) acting on the cell membrane as described below<sup>57</sup>.

The link force acts along the edge that connects two adjacent cell membrane vertices is representing the stretch force on the vertices as defined below:

$$F_{\text{link}} = -\frac{K_l k_B T (L_i - L_0)}{P L_0} \left[ 1 + \frac{1}{\tau_l^2 - \left(\frac{L_i - L_0}{L_0}\right)^2} \right] \quad (3)$$

where  $K_l$ ,  $k_B$ ,  $T$ ,  $L_i$ ,  $L_0$  are the link modulus, the Boltzmann constant, temperature, the current length of the edge, and the initial length of the edge, respectively.  $P = 7.5 \text{ nm}$  is the persistence-length of the edge, and  $\tau_l = 3$  is the relative expansion ratio at which the edge reaches its persistence length<sup>57</sup>.

The bending force is defined in terms of the change in the angles between the normal vectors of two adjacent surface elements as follows:

$$F_{\text{bend}} = -\frac{K_b k_B T (\theta_i - \theta_0)}{L_0} \left[ 1 + \frac{1}{\tau_b^2 - (\theta_i - \theta_0)^2} \right] \quad (4)$$

where  $K_b$ ,  $\theta_i$ , and  $\theta_0$  are the bending modulus, current and initial angles between the normal vectors of the surface elements, respectively.  $\tau_b$  is the limiting angle and is chosen to be  $\frac{\pi}{6}$  to prevent unrealistic sharp surface edges<sup>57</sup>.

The local area force applies on each surface element vertices and represents the reaction of the element to change of its area as follows:

$$F_{\text{area}} = -\frac{K_a k_B T A_i - A_0}{L_0 A_0} \left[ 1 + \frac{1}{\tau_a^2 - \left(\frac{A_i - A_0}{A_0}\right)^2} \right] \quad (5)$$

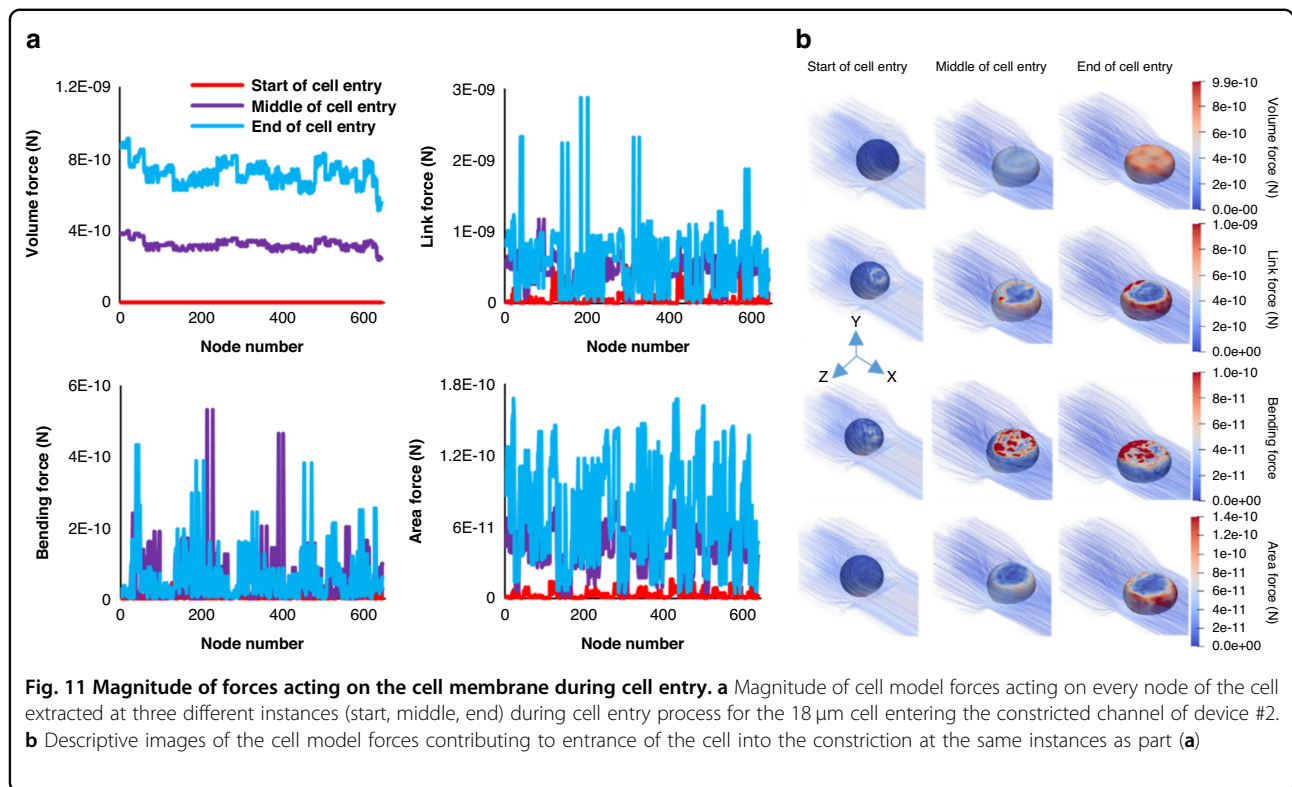
where  $K_a$ ,  $A_i$ , and  $A_0$  are the area modulus, the current and the initial area of the triangle, respectively.  $\tau_a = 0.3$  is the area limiting factor to prohibit surface area changes more than 30%<sup>57</sup>.

The global volume force applies on all vertices of the cell membrane and conserves the volume of the cell.

$$F_{\text{volume}} = -\frac{K_v k_B T \left(\frac{V_i - V_0}{V_0}\right)}{L_0} \left[ \frac{1}{\tau_v^2 - \left(\frac{V_i - V_0}{V_0}\right)^2} \right] \quad (6)$$

where  $K_v$ ,  $V_i$ , and  $V_0$  are the volume modulus the current and the initial volume of the cell membrane, respectively.  $\tau_v = 0.01$  is the volume limiting factor to resist changes in the cell volume<sup>57</sup>.

It worths noting that the cell model used in this study consists of 642 nodes on which all the mentioned forces



have been applied at every time step. Figure 11 illustrates the magnitude of the forces at three instances of cell entry process (start, middle, end) for 18  $\mu\text{m}$  cancer cell model entering the constricted channel of device #2. This figure shows all forces are at their minimum value before the cell deformation starts. For the most or all the vertices the values of the Volume forces, the Link forces, and the Area forces increase as the cell is squeezing to the constriction and reach to their maximum value at the end of the entry process. For the bending forces maximum values were reached during the cell squeezing. Figure 11b depicts the forces act on the cell membrane nodes at the mentioned instances by outputting the cell model during the entry process.

To achieve a realistic numerical model in this study, the internal viscosity of the cell was assumed to be different from the exterior fluid. Therefore, a dimensionless parameter named Viscosity Ratio (VR) was considered as follows:

$$VR = \frac{\text{Interior cell fluid viscosity}}{\text{the fluid viscosity}} \quad (7)$$

Therefore,  $K_l$ ,  $K_b$ ,  $K_a$ ,  $K_v$ , and  $VR$  are dimensionless parameters that need to be identified accurately to enable the numerical model to replicate the deformation behavior of the cancer cell captured in the correspondence experiment.

#### Fluid-solid interaction (FSI)

Here, fluid-cell interactions were modeled with Immerse Boundary Method (IBM) which acts as a bridge between Eulerian grids of the fluid and Lagrangian grids of the cell membrane<sup>68</sup>. More specifically, the exerted forces on the cell membrane nodes, determined by the cell's constitutive equations ( $F$ ), were spread on the fluid grids as follows:

$$f(x, t) = \int F(q, t)\delta(x - X(q, t))dq \quad (8)$$

where  $\delta$  is the Dirac delta function,  $x$  is the coordinate of the Eulerian grids, and  $X(q, t)$  is the position of a cell node with Lagrangian coordinate  $q$  at time  $t$ .

The velocity of the cell membrane nodes  $U(X(q, t))$  was obtained from the integral below and applied for updating the positions of the nodes.

$$U(X(q, t)) = \int u(x, t)\delta(x - X(q, t))dx \quad (9)$$

where  $u(x, t)$  is the velocity of the fluid with Eulerian grid  $x$  at time  $t$ .

#### Cell-wall interaction

Furthermore, repulsive forces were defined between the nodes of the cell and microchannel wall to avoid cell



penetration into the microchannel wall to model the behavior of the cell near the walls as:

$$\vec{F}_r(d) = \kappa_{rep} \frac{d_{cut}}{d} \vec{m}, d < d_{cut} \quad (10)$$

where  $\kappa_{rep}$  is the repulsion constant,  $d$  is the distance between the nodes of cell and wall,  $d_{cut}$  is the threshold of repulsive force activation, and  $\vec{m}$  is the unit vector pointing from the wall node to the cell node<sup>57</sup>. The repulsive-force parameters were constant in all simulations in this study (Table 3).

### Genetic algorithm (GA)

The mentioned parameters which describe the deformation behavior of the cancer cell were identified using the previously developed genetic algorithm<sup>8</sup>. This algorithm benefits from creating the first population of size 60 using randomly generated multi-digits binary numbers. Every 128 digits of the binary numbers represents one of the parameters and each row of the first population represents a set of parameters  $K_l$ ,  $K_b$ ,  $K_a$ ,  $K_v$ , and  $VR$ . Afterwards, every two rows of the first population were selected as parents and crossover has been performed for the crossover probability higher than a user-defined probability (0.8) for generating children. Then, mutation step was conducted for the mutation probability higher than a user-defined probability (0.6) on every digit of the binary numbers that made by crossover. The made children and the mutated ones were added to the previously generated first population. Then, the binary numbers were converted to decimal numbers according to the upper and lower bounds of each parameter as provided in Table 4. Then, using the decimal numbers, numerical simulations of the cancer cell entry process were performed in all three devices benefiting from parallel jobs on supercomputers. It is worth noting that every generation consisted of 120 sets of parameters, therefore, 360 simulations were performed simultaneously using 2 cores for each and the entry time was stored when the cells fully entered the constricted channels. For those simulations,

**Table 3 Parameters used in this study**

Parameters	Symbol	value	Unit
Time step	$\Delta t$	0.01	$\mu s$
Lattice resolution	$\Delta x$	1	$\mu m$
Fluid kinematic viscosity	$\nu$	$1.1 \times 10^{-6}$	$\frac{m^2}{s}$
Fluid density	$\rho$	1025	$\frac{kg}{m^3}$
Repulsive force activation threshold	$d_{cut}$	0.8	$\mu m$
Repulsive force scale coefficient	$\kappa_{rep}$	0.004	-

that the entry process took much longer than the experimental data, the simulations were stopped when the entry time reached a user-defined value (twice of the experimental data). Finally, the outcomes of the numerical simulations and the experimental data were compared based on the below error function:

$$\text{Error} = \sum_{n=1}^{n_t} E_n = \sum_{n=1}^{n_t} \left| 1 - \left( \frac{ET^s}{ET^e} \right)_n \right| \quad (11)$$

where  $E_n$ ,  $ET^s$ , and  $ET^e$  are the error in the  $n$ th device, numerically calculated entry time, and experimentally measured entry time, respectively. Here,  $n_t$  is equal to 3 for using the entry time at three different constricted devices.

At the end, the results for the parameters of the cell constitutive equations were sorted and the best 20 ones added to the initial population of the next generation. The algorithm stops if the error remains unchanged after 20 successive generations.

### Experimental setup

Before running the experiments, the devices were degassed for up to one day with Pluronic solution to avoid cell adhesion to the channels and washed with a constant flow of PBS for 20 min. The microfluidic device was placed on the stage of a Nikon Ti Eclipse inverted microscope in the experimental setup shown in Fig. 1a. The cell sample flowing in the media consisting of RPMI-1640 solution with 20% fetal bovine serum (FBS) (the media density  $\rho = 1020 \pm 5 \frac{kg}{m^3}$ , and the media dynamic viscosity  $\mu = 1.089 \pm 0.044 \text{ mPa s}$ )<sup>69</sup> with cell viability of % 90 or higher was infused into the constricted channel using a syringe pump (Chemyx Inc., USA) at a constant flow rate of 20  $\mu\text{L/h}$ . Cell samples with the concentration of  $2 \times 10^6$  cells per mL of media were prepared and used for all experiments. In addition, since the main focus of the present study is to validate the numerical model of single cancer cell deformation behavior, only the data of single cancer cells that pass the constricted channels one at a time have been gathered. More specifically, the captured data of cell clusters and more than one cells in the constricted channels at the same time were set aside from further analysis. At this flow rate, the entry time measured for the average cell size is less than 16 ms. The flow of

**Table 4 Upper bound and lower bound for cell model parameters**

	$K_b$	$K_v$	$K_a$	$K_l$	$VR$
Lower bound	0	0	0	0	0
Upper bound	$10^6$	$10^6$	$10^6$	$10^6$	40

cancer cells into the constricted channels has been visualized in bright field mode of the inverted microscope using a  $\times 20$  magnification objective and recorded using a high-speed camera (FASTCAM S1 model, Photon USA, Inc.) at a high frame rate of 5000 fps with the spatial resolution of  $512 \times 512$  pixels. All captured videos and images were analyzed manually using Photron Fastcam Viewer 4 (PFV4) software to measure cell size, entry time, and elongation index which is the ratio of cell length after entering the constriction to the original cell length. Figure 1b–d shows MDA-MB-231 cell squeezing and entering the microchannel sizes of 8, 10 and 12  $\mu\text{m}$ , respectively, at five instances until completion of cancer cell entry.

#### Acknowledgements

This work was supported by the Natural Sciences and Engineering Research Council of Canada (RGPIN-2020-05522 & RGPIN-2020-00428). We thank Dr. Mohammad Kohandel and Dr. Nafiseh Moghimi for providing cancer cell lines. This work was partly performed using the Giga-to-Nanoelectronics Centre facilities at the University of Waterloo. The simulations were performed using infrastructures of Digital Research Alliance of Canada ([www.alliancecan.ca](http://www.alliancecan.ca)). The authors thank Dr. John McPhee for providing access to high-speed imaging.

#### Author details

<sup>1</sup>Department of Systems Design Engineering, University of Waterloo, Waterloo, ON N2L 3G1, Canada. <sup>2</sup>Center for Bioengineering and Biotechnology, University of Waterloo, Waterloo, ON N2L 3G1, Canada. <sup>3</sup>Department of Electrical and Computer Engineering, University of Waterloo, Waterloo, ON N2L 3G1, Canada

#### Author contributions

P.K.M.: conceptualization, experimentation, experimental setup development, computational analysis, algorithm development, methodology, validation, interpretation of data, data analysis, data visualization writing – original draft and writing – review & editing. H.A.: experimentation, experimental setup development, cell culturing, methodology and writing – review & editing. M.P. and N.M.: conceptualization, interpretation of data, supervision, project administration, funding acquisition, writing – review & editing.

#### Conflict of interest

The authors declare no competing interests.

**Supplementary information** The online version contains supplementary material available at <https://doi.org/10.1038/s41378-023-00644-7>.

Received: 29 June 2023 Revised: 11 November 2023 Accepted: 27

November 2023

Published online: 12 January 2024

#### References

- Wirtz, D., Konstantopoulos, K. & Searson, P. C. The physics of cancer: the role of physical interactions and mechanical forces in metastasis. *Nat. Rev. Cancer* **11**, 512–522 (2011).
- Krog, B. L. & Henry, M. D. Biomechanics of the circulating tumor cell micro-environment. in *Biomechanics in Oncology*, 1092 (eds. Dong, C. et al.) 209–233 (Springer International Publishing, 2018).
- Ewing, J. Neoplastic diseases: a treatise on tumours. By James Ewing, A.M., M.D., Sc.D., Professor of Pathology at Cornell University Medical College, N.Y.; Pathologist to the Memorial Hospital. Third edition. Royal 8vo. Pp. 1127, with 546 illustrations. 1928. Philadelphia and London: W. B. Saunders Co. Ltd. 63s. net. *Br. J. Surg.* **16**, 174–175 (1928).
- Weiss, L., Bronk, J., Pickren, J. W. & Lane, W. W. Metastatic patterns and target organ arterial blood flow. *Invasion Metastasis* **1**, 126–135 (1981).
- Follain, G. et al. Hemodynamic forces tune the arrest, adhesion, and extravasation of circulating tumor cells. *Dev. Cell* **45**, 33–52.e12 (2018).
- Follain, G. et al. Fluids and their mechanics in tumour transit: shaping metastasis. *Nat. Rev. Cancer* **20**, 107–124 (2020).
- Poudineh, M. et al. Tracking the dynamics of circulating tumour cell phenotypes using nanoparticle-mediated magnetic ranking. *Nat. Nanotechnol.* **12**, 274–281 (2017).
- Keshavarz Motamed, P. & Maftoon, N. A systematic approach for developing mechanistic models for realistic simulation of cancer cell motion and deformation. *Sci. Rep.* **11**, 21545 (2021).
- Xiao, L. L., Yan, W. W., Liu, Y., Chen, S. & Fu, B. M. Modeling cell adhesion and extravasation in microvascular system. In *Molecular, Cellular, and Tissue Engineering of the Vascular System* (eds. Fu, B. M. & Wright, N. T.) 219–234 (Springer International Publishing, 2018).
- Dabagh, M. & Randles, A. Role of deformable cancer cells on wall shear stress-associated-VEGF secretion by endothelium in microvasculature. *PLoS ONE* **14**, e0211418 (2019).
- Anvari, S., Osei, E. & Maftoon, N. Interactions of platelets with circulating tumor cells contribute to cancer metastasis. *Sci. Rep.* **11**, 15477 (2021).
- Azevedo, A. S., Follain, G., Patthabhiraman, S., Harlepp, S. & Goetz, J. G. Metastasis of circulating tumor cells: Favorable soil or suitable biomechanics, or both?. *Cell Adh. Migr.* **9**, 345–356 (2015).
- Anvari, S., Nambiar, S., Pang, J. & Maftoon, N. Computational Models and Simulations of Cancer Metastasis. *Arch. Comput. Methods Eng.* <https://doi.org/10.1007/s11831-021-09554-1> (2021).
- Shen, J., Faruqi, A. H., Jiang, Y. & Maftoon, N. Mathematical reconstruction of patient-specific vascular networks based on clinical images and global optimization. *IEEE Access* **9**, 20648–20661 (2021).
- Borg, A., Paulsen Husted, B. & Njå, Ø. The concept of validation of numerical models for consequence analysis. *Reliab. Eng. Syst. Saf.* **125**, 36–45 (2014).
- Hou, H. W. et al. Deformability study of breast cancer cells using microfluidics. *Biomed. Microdevices* **11**, 557–564 (2009).
- Byun, S. et al. Characterizing deformability and surface friction of cancer cells. *Proc. Natl Acad. Sci. USA* **110**, 7580–7585 (2013).
- Chen, J. et al. Efficient extravasation of tumor-repopulating cells depends on cell deformability. *Sci. Rep.* **6**, 19304 (2016).
- Wang, S., Ye, T., Li, G., Zhang, X. & Shi, H. Margination and adhesion dynamics of tumor cells in a real microvascular network. *PLoS Comput. Biol.* **17**, e1008746 (2021).
- Puleri, D. F. & Randles, A. The role of adhesive receptor patterns on cell transport in complex microvessels. *Biomech. Model. Mechanobiol.* **21**, 1079–1098 (2022).
- Kienast, Y. et al. Real-time imaging reveals the single steps of brain metastasis formation. *Nat. Med.* **16**, 116–122 (2010).
- Humayun, M. et al. Elucidating cancer-vascular paracrine signaling using a human organotypic breast cancer cell extravasation model. *Biomaterials* **270**, 120640 (2021).
- Chaw, K. C., Manimaran, M., Tay, F. E. H. & Swaminathan, S. A quantitative observation and imaging of single tumor cell migration and deformation using a multi-gap microfluidic device representing the blood vessel. *Microvasc. Res.* **72**, 153–160 (2006).
- Rosenbluth, M. J., Lam, W. A. & Fletcher, D. A. Analyzing cell mechanics in hematologic diseases with microfluidic biophysical flow cytometry. *Lab Chip* **8**, 1062–1070 (2008).
- Au, S. H. et al. Clusters of circulating tumor cells traverse capillary-sized vessels. *Proc. Natl Acad. Sci. USA* **113**, 4947–4952 (2016).
- Anguiano, M. et al. Characterization of three-dimensional cancer cell migration in mixed collagen-Matrigel scaffolds using microfluidics and image analysis. *PLoS ONE* **12**, e0171417 (2017).
- Ren, X., Ghassemi, P., Babahosseini, H., Strobl, J. S. & Agah, M. Single-cell mechanical characteristics analyzed by multiconstriction microfluidic channels. *ACS Sens.* **2**, 290–299 (2017).
- Nath, B. et al. Understanding flow dynamics, viability and metastatic potency of cervical cancer (HeLa) cells through constricted microchannel. *Sci. Rep.* **8**, 17357 (2018).
- Poudineh, M. et al. Profiling functional and biochemical phenotypes of circulating tumor cells using a two-dimensional sorting device. *Angew. Chem.* **129**, 169–174 (2017).
- Rosendahl, P. et al. Real-time fluorescence and deformability cytometry. *Nat. Methods* **15**, 355–358 (2018).

31. Van der Meeren, L., Verduijn, J., Krysko, D. V. & Skirtach, A. G. High-throughput mechano-cytometry as a method to detect apoptosis, necroptosis, and ferroptosis. *Cell Prolif.* **56**, e13445 (2023).
32. Gossett, D. R. et al. Hydrodynamic stretching of single cells for large population mechanical phenotyping. *PNAS* **109**, 7630–7635 (2012).
33. Urbanska, M. et al. A comparison of microfluidic methods for high-throughput cell deformability measurements. *Nat. Methods* **17**, 587–593 (2020).
34. Osaki, T., Sivathanu, V. & Kamm, R. D. Vascularized microfluidic organ-chips for drug screening, disease models and tissue engineering. *Curr. Opin. Biotechnol.* **52**, 116–123 (2018).
35. Bagnall, J. S. et al. Deformability of tumor cells versus blood cells. *Sci. Rep.* **5**, 1–11 (2015).
36. Balogh, P., Gounley, J., Roychowdhury, S. & Randles, A. A data-driven approach to modeling cancer cell mechanics during microcirculatory transport. *Sci. Rep.* **11**, 15232 (2021).
37. Raj, A. & Sen, K. A. Entry and passage behavior of biological cells in a constricted compliant microchannel. *RSC Adv.* **8**, 20884–20893 (2018).
38. Raj, A., Dixit, M., Doble, M. & Sen, A. K. A combined experimental and theoretical approach towards mechanophenotyping of biological cells using a constricted microchannel. *Lab Chip* **17**, 3704–3716 (2017).
39. Zhou, C., Yue, P. & Feng, J. J. Simulation of neutrophil deformation and transport in capillaries using newtonian and viscoelastic drop models. *Ann. Biomed. Eng.* **35**, 766–780 (2007).
40. Harvie, D. J. E., Cooper-White, J. J. & Davidson, M. R. Deformation of a viscoelastic droplet passing through a microfluidic constriction. *J. Non Newton. Fluid Mech.* **155**, 67–79 (2008).
41. Leong, F. Y., Li, Q., Lim, C. T. & Chiam, K.-H. Modeling cell entry into a micro-channel. *Biomech. Model. Mechanobiol.* **10**, 755–766 (2011).
42. Shirai, A. & Masuda, S. Numerical simulation of passage of a neutrophil through a rectangular channel with a moderate constriction. *PLoS ONE* **8**, e59416 (2013).
43. Moon, J. Y., Tanner, R. I. & Lee, J. S. A numerical study on the elastic modulus of volume and area dilation for a deformable cell in a microchannel. *Biomicrofluidics* **10**, 044110 (2016).
44. Xiao, L. L., Liu, Y., Chen, S. & Fu, B. M. Numerical simulation of a single cell passing through a narrow slit. *Biomech. Model. Mechanobiol.* **15**, 1655–1667 (2016).
45. Tan, J., Sohrabi, S., He, R. & Liu, Y. Numerical simulation of cell squeezing through a micropore by the immersed boundary method. *Proc. Inst. Mech. Eng. Part C J. Mech. Eng. Sci.* **232**, 502–514 (2018).
46. Zhou, L., Feng, S., Liu, H. & Chang, J. Dissipative particle dynamics simulation of cell entry into a micro-channel. *Eng. Anal. Bound. Elem.* **107**, 47–52 (2019).
47. Lim, C. T., Zhou, E. H. & Quek, S. T. Mechanical models for living cells—a review. *J. Biomech.* **39**, 195–216 (2006).
48. Luo, Y. N. et al. A constriction channel based microfluidic system enabling continuous characterization of cellular instantaneous Young's modulus. *Sens. Actuators B Chem.* **202**, 1183–1189 (2014).
49. Reasor, D. A., Clausen, J. R. & Aidun, C. K. Coupling the lattice-Boltzmann and spectrin-link methods for the direct numerical simulation of cellular blood flow. *Int. J. Numer. Methods Fluids* **68**, 767–781 (2012).
50. Mokbel, M. et al. Numerical simulation of real-time deformability cytometry to extract cell mechanical properties. <https://pubs.acs.org/doi/pdf/10.1021/acsbiomaterials.6b00558> (2017).
51. Müller, S. J. et al. A hyperelastic model for simulating cells in flow. *Biomech. Model. Mechanobiol.* **20**, 509–520 (2021).
52. Ye, T., Phan-Thien, N. & Lim, C. T. Particle-based simulations of red blood cells—a review. *J. Biomech.* **49**, 2255–2266 (2016).
53. Discher, D. E., Boal, D. H. & Boey, S. K. Simulations of the erythrocyte cytoskeleton at large deformation. II. Micropipette aspiration. *Biophys. J.* **75**, 1584–1597 (1998).
54. Dao, M., Lim, C. T. & Suresh, S. Mechanics of the human red blood cell deformed by optical tweezers. *J. Mech. Phys. Solids* **51**, 2259–2280 (2003).
55. Fedosov, D. A., Caswell, B. & Karniadakis, G. E. A multiscale red blood cell model with accurate mechanics, rheology, and dynamics. *Biophys. J.* **98**, 2215–2225 (2010).
56. Cimrak, I. & Jancigova, I. *Computational Blood Cell Mechanics: Road Towards Models and Biomedical Applications* (CRC Press, 2018).
57. Závadoszky, G., van Rooij, B., Azizi, V. & Hoekstra, A. Cellular level in-silico modeling of blood rheology with an improved material model for red blood cells. *Front. Physiol.* **8**, 563 (2017).
58. Ye, T., Shi, H., Phan-Thien, N., Lim, C. T. & Li, Y. Relationship between transit time and mechanical properties of a cell through a stenosed microchannel. *Soft Matter* **14**, 533–545 (2018).
59. Dao, M., Li, J. & Suresh, S. Molecularly based analysis of deformation of spectrin network and human erythrocyte. *Mater. Sci. Eng. C* **26**, 1232–1244 (2006).
60. Pivkin, I. V. & Karniadakis, G. E. Accurate coarse-grained modeling of red blood cells. *Phys. Rev. Lett.* **101**, 118105 (2008).
61. Dupin, M. M., Halliday, I., Care, C. M., Alboul, L. & Munn, L. L. Modeling the flow of dense suspensions of deformable particles in three dimensions. *Phys. Rev. E* **75**, 066707 (2007).
62. MacMECCAN, R. M., Clausen, J. R., Neitzel, G. P. & Aidun, C. K. Simulating deformable particle suspensions using a coupled lattice-Boltzmann and finite-element method. *J. Fluid Mech.* **618**, 13–39 (2009).
63. Omori, T. et al. Comparison between spring network models and continuum constitutive laws: Application to the large deformation of a capsule in shear flow. *Phys. Rev. E* **83**, 041918 (2011).
64. Jančígová, I., Kovalčíková, K., Bohiníková, A. & Cimrák, I. Spring-network model of red blood cell: from membrane mechanics to validation. *Int. J. Numer. Methods Fluids* **92**, 1368–1393 (2020).
65. Freund, A. et al. IL-8 expression and its possible relationship with estrogen-receptor-negative status of breast cancer cells. *Oncogene* **22**, 256–265 (2003).
66. Latt, J. et al. Palabos: parallel lattice Boltzmann solver. *Comput. Math. Appl.* <https://doi.org/10.1016/j.camwa.2020.03.022> (2020).
67. Bergeaud, V. & Lefebvre, V. SALOME. A software integration platform for multi-physics, pre-processing and visualisation. <https://www.osti.gov/etdeweb/biblio/21575789> (2010).
68. Peskin, C. S. The immersed boundary method. *Acta Numerica* **11**, 479–517 (2002).
69. Poon, C. *Measuring the density and viscosity of culture media for optimized computational fluid dynamics analysis of in vitro devices*. <http://biorxiv.org/lookup/doi/10.1101/2020.08.25.266221> (2020).